Research Square

Preprints are preliminary reports that have not undergone peer review.
They should not be considered conclusive, used to inform clinical practice,
or referenced by the media as validated information.

Data-anchored multistage mechanistic modelling of Ni-BTC- modified TiO_2 aerogel photoanodes for dye-sensitised solar cells

E. R. Anishiya Chella Daisy
Arunachala Hitech Engineering College
P. Ram Kumar
dr.ramchem93@gmail.com

Thiagarajar College of EngineeringDe
X. Sahaya Shajan
Gregorian Institute of Technology

Research Article

Keywords: dye-sensitized solar cells, TiO_2 aerogel, Ni-BTC, metal–organic framework, electrochemical impedance spectroscopy, charge transport

Posted Date: November 13th, 2026

DOI: https://doi.org/10.21203/rs.3.rs-11553354/v1

License: This work is licensed under a Creative Commons Attribution 4.0 International License.
Read Full License

Additional Declarations: No competing interests reported.

Data-anchored multistage mechanistic modelling of Ni-BTC-modified TiO_2 aerogel photoanodes for dye-sensitised solar cells

E. R. Anishiya Chella Daisy[a], P. Ram Kumar[b*], X. Sahaya Shajan[c]

[a]*Department of Chemistry, Arunachala Hitech Engineering College, Kanyakumari – Tamil Nadu, India.*

[b]*Advanced Materials Lab-Centre of Excellence in Hydrogen Energy Research, Department of Chemistry, Thiagarajar College of Engineering, Madurai – 625 015, Tamil Nadu, India.*

[c]*Department of Physics, Gregorian Institute of Technology, Kangazha, Kottayam – 686556, Kerala. India.*

Corresponding author: Dr P. Ram Kumar, dr.ramchem93@gmail.com

Abstract

Dye-sensitised solar-cell photoanodes exhibit coupled optical, interfacial and charge-transport processes, making it difficult to assign photovoltaic improvement to a single material descriptor. Here, a data-anchored multistage modelling framework was developed for TiO_2 aerogel photoanodes containing 0–0.75 wt% Ni-BTC metal–organic framework (MOF), using the experimental dataset of Ramasubbu et al. as locked calibration and validation anchors. The workflow combines structural interpolation, band-gap and optical-generation descriptors, N719 injection energetics, electrochemical-impedance-derived transport and recombination descriptors, a reduced device-level *J–V* model, composition-specific digital twins, continuous composition optimisation, sensitivity analysis and Monte Carlo uncertainty propagation. The experimentally measured maximum power-conversion efficiency (PCE) of 8.846% at 0.50 wt% Ni-BTC coincides with the lowest interfacial resistance R_2 (9.81 Ω), a 1.1617 ms electron lifetime and the highest normalised transport descriptor τ_n/R_2. In contrast, 0.25 wt% exhibits the highest modelled injection index but a lower J_{sc}, demonstrating that charge generation alone does not determine device output. At 0.75 wt%, the lifetime increases to 1.4601 ms, but R_2 and R_3 rise to 54.3 and 96.1 Ω, respectively, producing a severe transport penalty and reducing PCE to 4.353%. Monte Carlo propagation retained 0.50 wt% as the PCE optimum in all 10,000 realisations under the stated uncertainty assumptions. The framework therefore identifies interfacial resistance and coupled transport as dominant design variables and provides a reproducible route for prospective experimental validation of optimised MOF–TiO_2 photoanodes.

Keywords: dye-sensitized solar cells; TiO_2 aerogel; Ni-BTC; metal–organic framework; electrochemical impedance spectroscopy; charge transport

1. Introduction

Dye-sensitised solar cells (DSSCs) remain an important class of sensitised photovoltaic devices because their operating mechanism separates light harvesting from charge collection: a molecular sensitiser absorbs incident photons, injects electrons into a mesoporous semiconductor, and a redox mediator regenerates the oxidised sensitiser [1, 2]. This architecture allows considerable freedom in choosing the sensitiser, semiconductor morphology, electrolyte, and interfaces, and has supported low-cost, flexible, low-light photovoltaic concepts [2,3]. Nevertheless, device output depends on a chain of coupled events rather than optical absorption alone. Electron injection, transport through the mesoporous semiconductor, interfacial recombination, electrolyte regeneration, and ionic diffusion collectively determine J_{sc}, V_{oc}, and FF, and therefore the final PCE [3–5].

TiO_2 remains the most extensively studied DSSC photoanode because of its chemical stability, suitable conduction-band position, abundance and compatibility with sensitiser chemistry. The classical nanocrystalline TiO_2 architecture laid the foundation for modern DSSCs, while subsequent work has shown that particle size, pore architecture, surface chemistry, light scattering, and interfacial passivation strongly influence device performance [2,4]. Three-dimensional TiO_2 aerogels are particularly attractive because their interconnected pore–solid networks can simultaneously provide high internal surface area, dye immobilisation sites and pathways for electrolyte penetration and electron transport. Pietron et al. demonstrated the photovoltaic utility of dye-sensitised titania aerogels, establishing the relevance of bicontinuous porous architectures for sensitised solar-energy conversion [7].

Consequently, modifying TiO_2 through doping, compositing, and interfacial engineering has become a major strategy for overcoming the intrinsic limitations of mesoporous photoanodes. A recent review in this journal emphasises that photoanode modification can alter the optical gap, charge-transfer resistance and carrier lifetime, but also stresses that excessive modification can degrade photovoltaic performance [5]. Independent studies of Ni-modified TiO_2 likewise show that an optimum dopant concentration can improve visible-light harvesting, dye adsorption and charge transport, whereas the response depends strongly on the preparation route and loading level [6]. More generally, photoanode optimisation strategies include nanoarchitecture, light scattering, compositing, doping and surface/interfacial engineering [4,9].

Metal–organic frameworks (MOFs) offer a distinctive route to photoanode engineering because their metal nodes and organic linkers generate tunable coordination environments and porous structures. In

hybrid systems, MOFs need not function as the primary electron-transport phase; instead, they can act as secondary porous or interfacial components that modify surface chemistry, local electronic structure and transport pathways. MOF/aerogel composites are especially interesting because they can combine multiple pore scales and create hierarchical architectures [8]. However, incorporating MOFs introduces a fundamental optimisation problem: increasing MOF content may improve some optical or interfacial descriptors while simultaneously blocking pores, increasing tortuosity, reducing dye uptake, or increasing charge-transfer resistance. Thus, one descriptor alone cannot reliably explain the experimentally observed optimum.

The parent experimental study by Ramasubbu et al. provides an unusually suitable dataset for addressing this problem [1]. TiO_2–Ni-MOF composite aerogels were prepared with Ni-MOF contents of 0, 0.25, 0.50 and 0.75 wt%, and the corresponding devices showed PCE values of 6.805, 7.950, 8.846 and 4.353%, respectively. The 0.50 wt% device also exhibited the highest J_{sc} (27.32 mA cm^{-2}) and the lowest reported R_2 (9.81 Ω), while the 0.75 wt% device displayed a much larger R_2 (54.3 Ω) and R_3 (96.1 Ω) despite having the longest impedance-derived lifetime. These observations suggest a non-monotonic competition between charge generation, interfacial transfer, recombination and ionic transport [1].

The present work therefore does not introduce a new experimental material dataset. Instead, it develops a transparent, data-anchored mechanistic model from the published experimental anchors. The specific objectives are to (i) establish a common parameter database; (ii) connect composition to structural and optical descriptors; (iii) quantify N719 injection and EIS-derived transport/recombination descriptors; (iv) construct composition-specific digital twins and a reduced device-level *J–V* model; (v) determine the continuous composition landscape between experimental anchors; and (vi) quantify sensitivity and uncertainty and define a prospective validation protocol. The central hypothesis is that the experimentally observed 0.50 wt% optimum is a balanced state in which interfacial charge transfer and electron transport compensate for the non-monotonic changes in dye loading and optical response.

2 Materials and methods

2.1 Experimental data provenance

All experimental anchor values used in this modelling study were taken from the parent experimental paper by Ramasubbu et al. [1]. The parent study synthesised TiO_2–Ni-MOF composite aerogels via a sol–gel route, varied Ni-MOF loading from 0 to 0.75 wt%, characterised structural, optical, surface, and electrochemical properties, and fabricated quasi-solid DSSCs. The reported EIS measurements

were acquired under 50 mW cm^{-2} illumination over 100 mHz–100 kHz with a 5 mV perturbation, and the equivalent circuit contained series resistance and three interfacial/diffusion contributions [1]. The present model introduced no unreported CPE values, mobility values, absolute absorption coefficients, or film thicknesses.

The four composition anchors were treated as locked observations rather than adjustable fitting points. This distinction is important because several model outputs below are interpolations or derived descriptors rather than independent measurements. The evidence classes used throughout the study are: measured (reported directly in [1]); derived (calculated algebraically from measured quantities); modelled/digitized (obtained from an explicit modelling or digitisation assumption); interpolated (estimated between experimental anchors); and assumed (external parameter required because the parent dataset did not report it).

2.2 Multistage modelling workflow

The complete workflow is summarised in Fig. 1. Experimental anchors were first assembled into a master database, after which each modelling stage was propagated without overwriting the measured values.

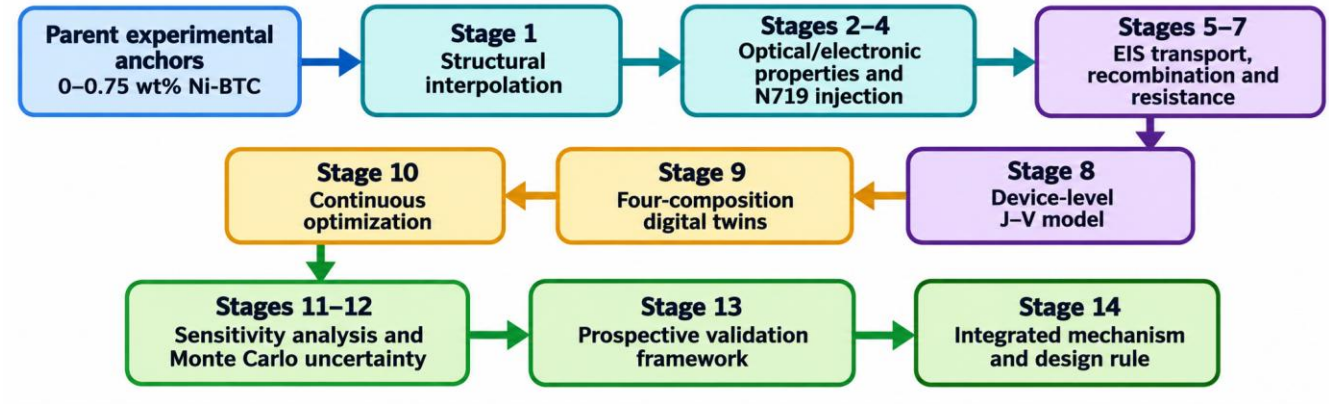


Fig. 1 Data-anchored multistage workflow used to connect Ni-BTC composition with structure, optical/electronic descriptors, interfacial transfer, charge transport, recombination and photovoltaic output.

Stage 1 used shape-preserving piecewise cubic Hermite interpolation (PCHIP) to describe continuous structural evolution between the four measured compositions. Stage 2 converted the measured optical band gaps into absorption-edge wavelengths using $\lambda_g = 1240/E_g$ and used digitised published UV–Vis trends to construct a normalised optical-generation proxy; absolute photon-generation rates were

intentionally not claimed because the parent dataset does not provide absolute α(λ) and photoanode thickness. Stage 3 used digitized/modelled conduction-band descriptors and an assumed N719 LUMO of −3.90 eV to define a relative injection-driving-force term. Stage 4 combined normalised optical, dye-loading and injection-driving-force factors into a relative photon-to-electron injection index.

Stages 5–7 were anchored primarily to EIS. Electron lifetime was calculated from the reported Bode-plot maximum frequency as $\tau_n = 1/(2\pi f_{max})$. A transport descriptor was then defined as $\Psi_{tr} = \tau_n/R_2$ and normalized to the pristine device. We treated R_2 as the principal dye/TiO_2/electrolyte interfacial resistance, while R_3 represented the low-frequency ionic-diffusion contribution, following the parent paper. The recombination-rate descriptor was $k_{rec} = 1/\tau_n$. Total and interfacial resistance metrics were calculated algebraically from the reported EIS elements. Stage 8 employed a reduced single-diode representation, $J = J_{sc} - J_0\left[\exp\left(\frac{V+JR_{s,\mathrm{eff}}}{nV_t}\right) - 1\right]$, with T = 298.15 K and $n = 1$. The measured Jsc and Voc were retained as boundary conditions because absolute generation, injection yield and transport coefficients were unavailable. A single global scaling factor converted the measured EIS series resistance into an effective device resistance and was calibrated only against the pristine FF. Consequently, modelled FF and PCE are not independent experimental predictions and are reported as retrospective forward-model outputs.

Stage 9 represented each composition as a digital twin state vector. Stage 10 used PCHIP to construct a continuous 0–0.75 wt% composition landscape. The continuous PCE curve is therefore an interpolation of the measured PCE anchors and should not be interpreted as a new experimental prediction. Stage 11 quantified rank-based and linear sensitivity. Stage 12 propagated stated relative uncertainties through 10,000 Monte Carlo realizations. Stage 13 defined a locked prospective validation experiment at 0.35, 0.45, 0.50, 0.55 and 0.65 wt%. Stage 14 integrated the results into a mechanistic state-transition model.

2.3 Quantitative descriptors and validation metrics

The principal transport descriptor was selected because τ_n alone does not account for the ease of interfacial charge transfer. Thus, $\Psi_{tr} = \frac{\tau_n/R_2}{\tau_{n,0}/R_{2,0}}$, where subscript 0 denotes the pristine device. Relative injection was calculated from the product of normalized optical, dye-loading and injection-driving-force factors. Model performance was assessed using root-mean-square error (RMSE), mean absolute error (MAE), mean absolute percentage error (MAPE) and coefficient of determination (R^2). Sensitivity was evaluated using Pearson and Spearman correlations. These statistics are descriptive for the four-anchor dataset and should not be interpreted as population-level estimates. Monte Carlo

propagation used 10,000 realisations with assumed relative uncertainties of 2% for PCE and Jsc, 5% for R_2, 3% for fmax, 5% for injection index and 5% for the transport descriptor. A 70:30 mixture of PCHIP and piecewise-linear interpolation represented model-form uncertainty. These uncertainty values were not reported as measurement error bars in the parent study and are therefore explicitly treated as modelling assumptions.

3. Results and discussion

3.1 Experimental anchor landscape

The experimentally reported structural, optical, electrochemical, and photovoltaic parameters for the four Ni-BTC loading compositions were compiled to establish the reference dataset for the multistage mechanistic modelling framework. These experimentally measured values serve as fixed calibration and validation anchors for the subsequent analyses, as summarised in Table 1. The experimental anchor landscape reveals a non-monotonic response. Crystallite size decreases continuously from 8.5 to 5.7 nm as Ni-BTC increases, while the band gap decreases from 3.00 to 2.79 eV at 0.50 wt% and then slightly increases to 2.85 eV. BET surface area reaches 269 $m^2 g^{-1}$ at 0.25 wt% but decreases to 233 $m^2 g^{-1}$ at 0.75 wt%. The photovoltaic response is similarly non-monotonic, with 0.50 wt% providing the maximum J_{sc} and PCE. These trends are shown graphically in Figs. 2 and 3.

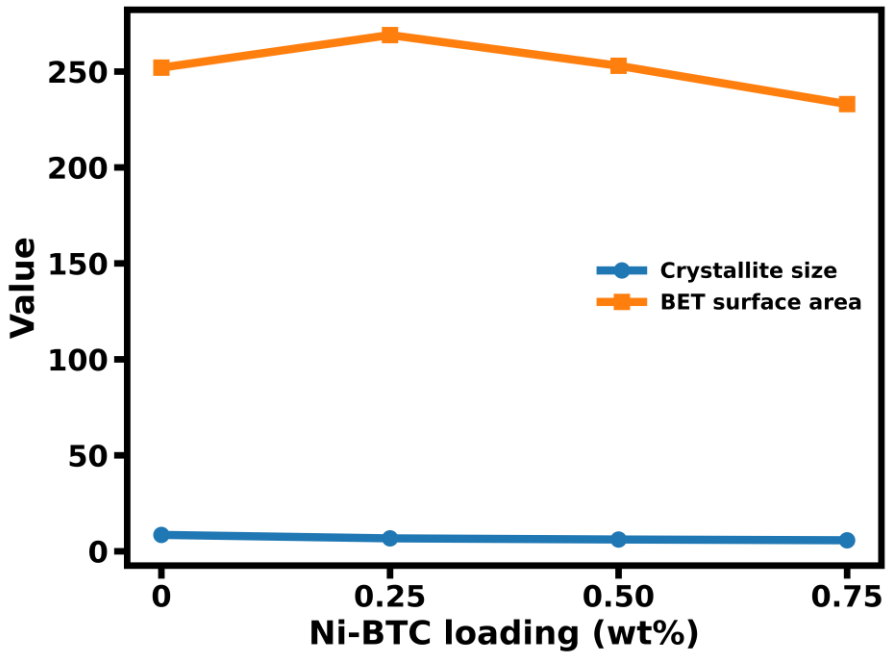


Fig. 2 Structural evolution across the experimental composition anchors: crystallite size and band gap as functions of Ni-BTC loading.

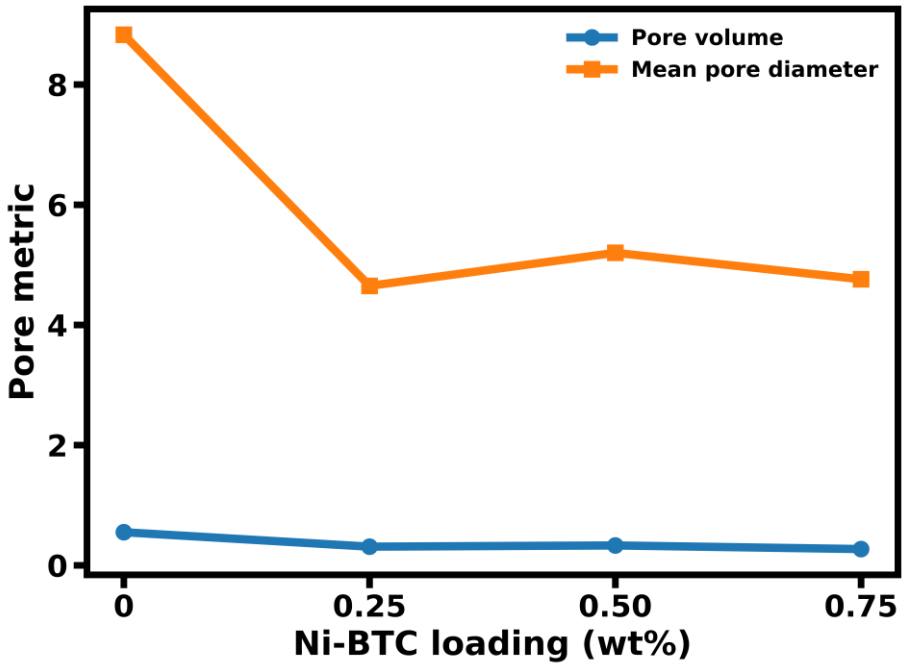


Fig. 3 Evolution of BET surface area, pore volume, and mean pore diameter with Ni-BTC loading.

Table 1 Experimental anchor parameters adopted from the parent study [1].

Ni-BTC (wt%)	Crystallite size (nm)	Eg (eV)	BET (m^2 g^{-1})	Pore volume (cm^3 g^{-1})	Mean pore diameter (nm)	Dye loading (10^{-3} mmol mg^{-1})	J_{sc} (mA cm^{-2})	V_{oc} (V)	FF	PCE (%)
0	8.5	3.00	252	0.55	8.83	0.95	20.07	0.638	0.528	6.805
0.25	6.7	2.80	269	0.31	4.65	1.08	23.65	0.627	0.533	7.950
0.50	6.1	2.79	253	0.33	5.20	0.88	27.32	0.624	0.516	8.846
0.75	5.7	2.85	233	0.27	4.76	0.77	12.48	0.605	0.576	4.353

3.2 Interfacial resistance and charge-transport regime

To elucidate the influence of Ni-BTC loading on interfacial charge transfer and electrolyte-related transport, the EIS-derived resistance components (R_s), (R_1), (R_2), and (R_3) were compared across the four compositions. Fig. 4 shows the variation in these resistance components. The most pronounced electrochemical change occurs in R_2. It decreases from 25.7 Ω in the pristine device to 11.2 and 9.81 Ω at 0.25 and 0.50 wt%, respectively, then increases sharply to 54.3 Ω at 0.75 wt%. R_3 follows the same qualitative failure at high loading, increasing to 96.1 Ω. The combined interfacial resistance $R1 + R2$ reaches a minimum at 0.50 wt%, while total resistance rises dramatically at 0.75 wt%. These results reproduce the central qualitative interpretation of the parent study and provide a quantitative basis for the transport descriptor used here [1].

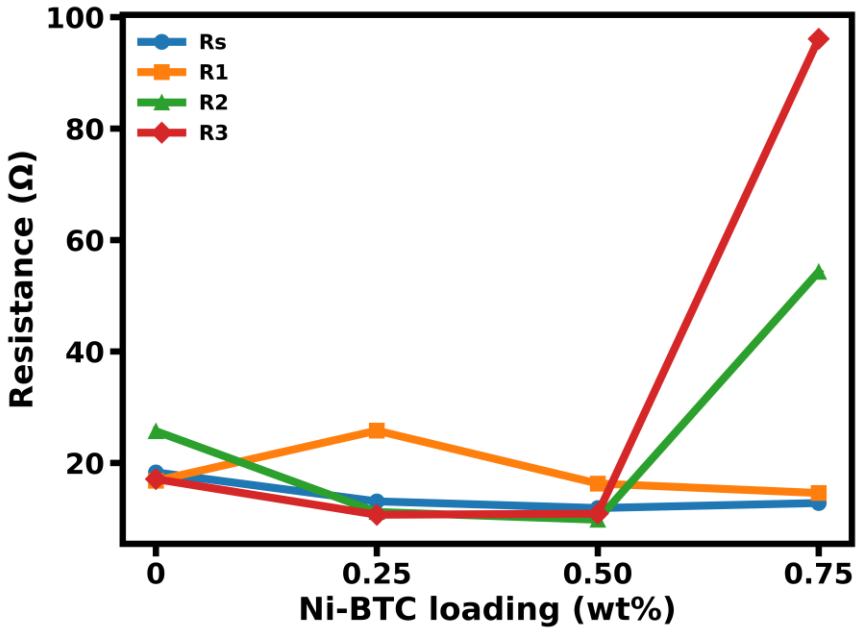


Fig. 4. EIS resistance components and composite resistance metrics derived from the parent equivalent-circuit parameters [1].

Table 2. EIS-derived resistance and lifetime descriptors

Ni-BTC (wt%)	Rs (Ω)	R1 (Ω)	R2 (Ω)	R3 (Ω)	R1+R2 (Ω)	R_{total} (Ω)	τ_n (ms)
0	18.30	16.80	25.70	17.10	42.50	77.90	0.9253
0.25	13.10	25.80	11.20	10.70	37.00	60.80	1.1617
0.50	11.90	16.30	9.81	10.90	26.11	48.91	1.1617
0.75	12.80	14.60	54.30	96.10	68.90	177.80	1.4601

To further investigate the influence of Ni-BTC loading on charge-carrier dynamics, the electron lifetime (τ_n) and corresponding recombination rate were derived from the characteristic frequency obtained from the EIS Bode plots. The composition-dependent variations in these parameters are presented in Fig. 5. As shown in Fig. 5, the electron lifetime increases from 0.925 ms for pristine TiO_2 to 1.162 ms at 0.25 and 0.50 wt% Ni-BTC, reaching 1.460 ms at 0.75 wt%. The corresponding EIS-derived recombination rate ($k_{rec}=1/\tau_n$) decreases from 1080.7 to 860.8 s^{-1} at 0.25 and 0.50 wt%, and further to 684.9 s^{-1} at 0.75 wt%. These trends suggest slower characteristic recombination kinetics with increasing Ni-BTC loading. However, the longest lifetime at 0.75 wt% does not translate into superior photovoltaic performance, as this composition exhibits substantially higher interfacial resistance R_2 = 54.3 Ω and electrolyte-related resistance R_3=96.1 Ω. Therefore, electron lifetime alone is insufficient to

explain device performance; interfacial charge transfer and transport limitations must also be considered.

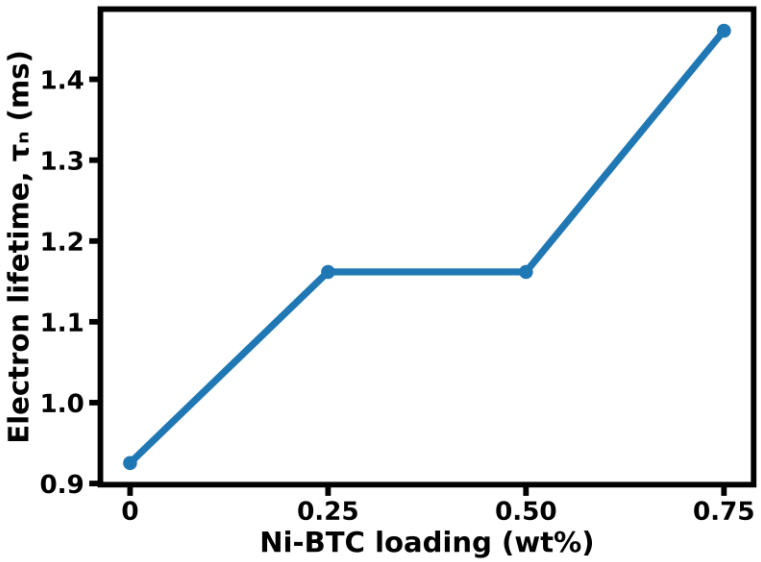


Fig. 5 EIS-derived electron lifetime τ_n and recombination-rate descriptor $k_{rec} = 1/\tau_n$

3.3 Optical and injection descriptors

The optical and electronic descriptors of the four Ni-BTC compositions were further evaluated to understand their potential influence on photon harvesting and electron injection into the TiO_2 conduction band. The estimated absorption-edge wavelengths, relative optical-generation factors, dye-loading values, and model-derived injection driving forces are summarized in Table 3. These parameters provide the basis for comparing the relative injection behaviour of the compositions in the subsequent mechanistic analysis. The relative injection index increases strongly at 0.25 wt% because the optical, dye-loading and assumed injection-driving-force terms reinforce one another. It remains elevated at 0.50 wt% and decreases at 0.75 wt%. Importantly, the 0.25 wt% sample has a larger injection index than the 0.50 wt% sample but a lower measured Jsc. This divergence is mechanistically useful: it demonstrates that charge generation/injection is not sufficient to determine current collection, and that the downstream transport pathway must be included. Figure 6 summarises the model-derived injection and transport descriptors.

Table 3 Optical/injection descriptors used in the forward modelling chain.

Ni-BTC (wt%)	Relative optical factor	Relative injection index	Dye loading (10^{-3} mmol mg^{-1})	Eg (eV)
0	1.000	1.000	0.95	3.00

0.25	1.513	5.160	1.08	2.80
0.50	1.536	4.316	0.88	2.79
0.75	1.383	3.176	0.77	2.85

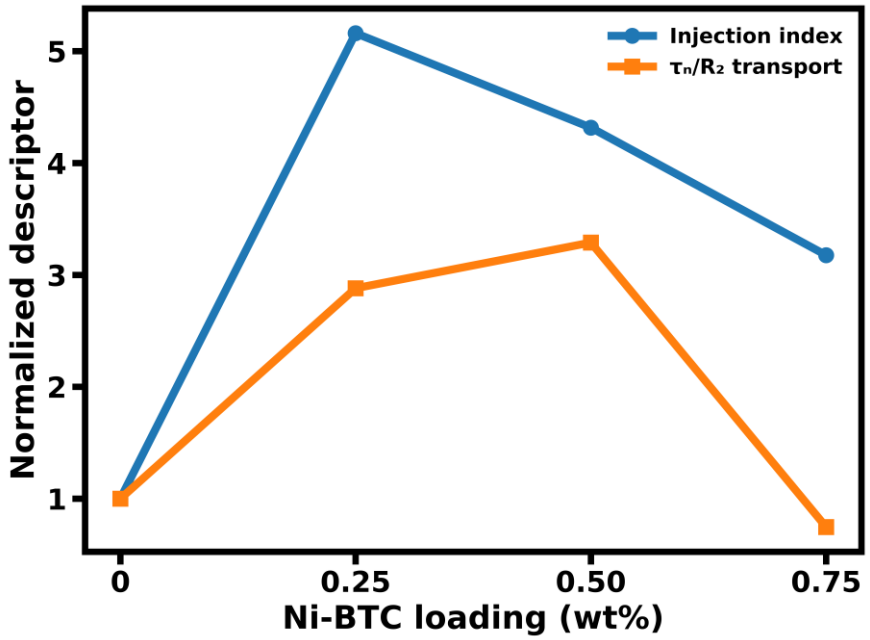


Fig. 6 Relative photon-to-electron injection and EIS-derived transport descriptors across Ni-BTC loading.

3.4 Transport descriptor and photovoltaic response

The transport and interfacial charge-transfer descriptors were further analysed to clarify the relationship between electron lifetime, interfacial resistance, and photovoltaic performance in the Ni-BTC-modified TiO_2 aerogel photoanodes. The composition-dependent transport descriptors and associated resistance parameters are summarized in Table 4. These parameters provide a comparative basis for assessing the balance between electron transport and interfacial charge transfer and for interpreting the experimentally observed optimum at 0.50 wt% Ni-BTC. The normalized transport descriptor $\tau n/R_2$ increases from 1.00 for pristine TiO_2 to 2.88 at 0.25 wt% and 3.29 at 0.50 wt%, before collapsing to 0.747 at 0.75 wt%. The descriptor therefore captures a key feature missed by lifetime alone: 0.75 wt% has the longest lifetime but the poorest transport state because its interfacial resistance is extremely high. Across the four anchors, the Pearson correlation between τ_n/R_2 and Jsc is approximately 0.899, while the corresponding Pearson correlation with PCE is approximately 0.892. Spearman rank

correlations are +1.00 for both Jsc and PCE, although the sample size is only four. Figure 7 shows the direct relationship between the transport descriptor and measured J_{sc}.

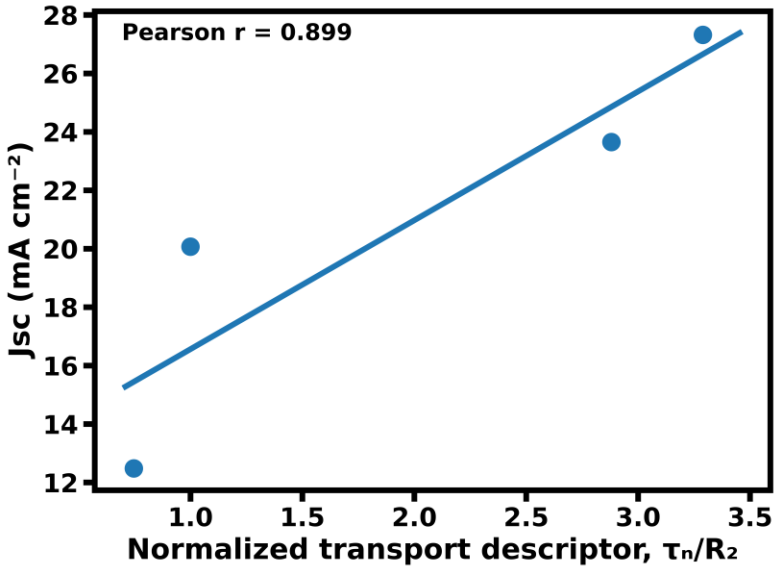


Fig. 7 Relationship between the normalised transport descriptor τ_n/R_2 and measured short-circuit current density. The regression is descriptive for the four experimental anchors.

Table 4 Integrated mechanistic descriptors and photovoltaic response.

Ni-BTC (wt%)	Injection index	τ_n/R_2 transport descriptor	Jsc (mA cm^{-2})	PCE (%)
0	1.000	1.000	20.07	6.805
0.25	5.160	2.881	23.65	7.950
0.50	4.316	3.289	27.32	8.846
0.75	3.176	0.747	12.48	4.353

Sensitivity analysis further supports the dominant role of interfacial resistance. R_2 shows the strongest negative rank association with both *Jsc* and PCE (Spearman $\rho = -1.00$), whereas the transport descriptor shows the strongest positive association. Lifetime alone is comparatively weak because the longest lifetime occurs at 0.75 wt%, where transport is severely compromised. R_3 also becomes strongly unfavourable at the highest loading, indicating that ionic diffusion contributes to the high-loading failure regime.

3.5 Photovoltaic performance and device-level model

To further evaluate the influence of Ni-BTC loading on the photovoltaic response, the composition-dependent current density–voltage characteristics and the corresponding device performance

parameters were analysed. The relevant photovoltaic metrics, including short-circuit current density (Jsc), open-circuit voltage (Voc), fill factor (FF), and power conversion efficiency (PCE), are summarized in Table 5. This comparison helps identify the optimum Ni-BTC loading by considering the combined effects of charge generation, charge collection, and interfacial and transport losses. The photovoltaic response exhibits a clear non-monotonic dependence on Ni-BTC loading (Fig. 8). J_{sc} increases from 20.07 mA cm^{-2} for pristine TiO_2 to 23.65 and 27.32 mA cm^{-2} at 0.25 and 0.50 wt%, respectively, while V_{oc} decreases slightly from 0.638 to 0.624 V. The 0.50 wt% electrode therefore achieves the highest photocurrent, indicating more efficient charge generation and collection despite its lower dye loading than the 0.25 wt% electrode. This behaviour is consistent with its lower R_2 (9.81 Ω) and longer electron lifetime (1.162 ms). At 0.75 wt%, J_{sc} drops sharply to 12.48 mA cm^{-2}, despite FF increasing to 0.576 (Fig. 8). This deterioration is accompanied by large increases in R_2 and R_3, indicating severe interfacial and transport limitations. Consequently, the PCE increases from 6.805% to a maximum of 8.846% at 0.50 wt%, followed by a sharp decrease to 4.353% at 0.75 wt% (Fig. 9). Overall, the results demonstrate that 0.50 wt% Ni-BTC provides the most favourable balance between charge generation, interfacial transfer and electron transport, establishing it as the experimentally observed optimum composition.

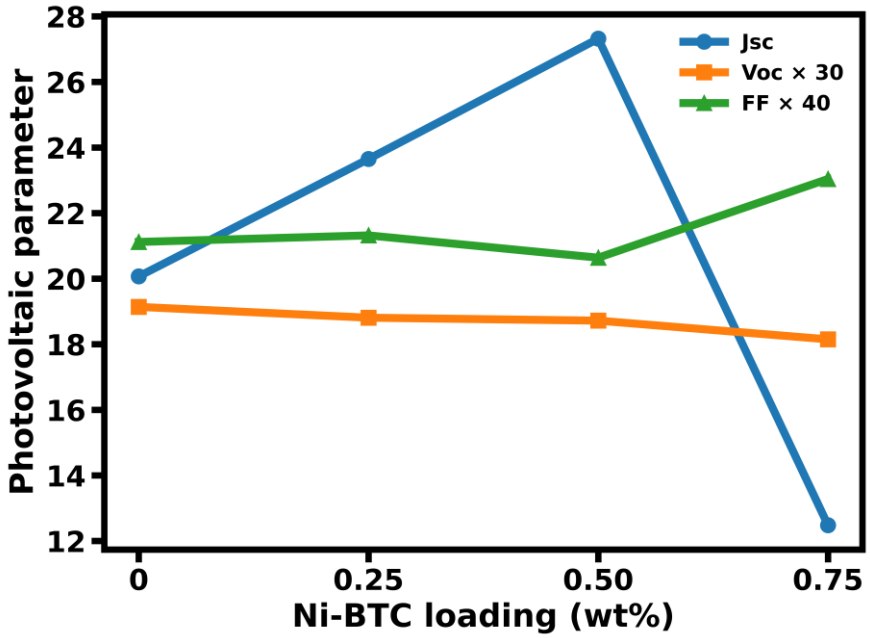


Fig. 8 Experimental photovoltaic parameters J_{sc}, V_{oc}, FF and PCE as functions of Ni-BTC loading [1].

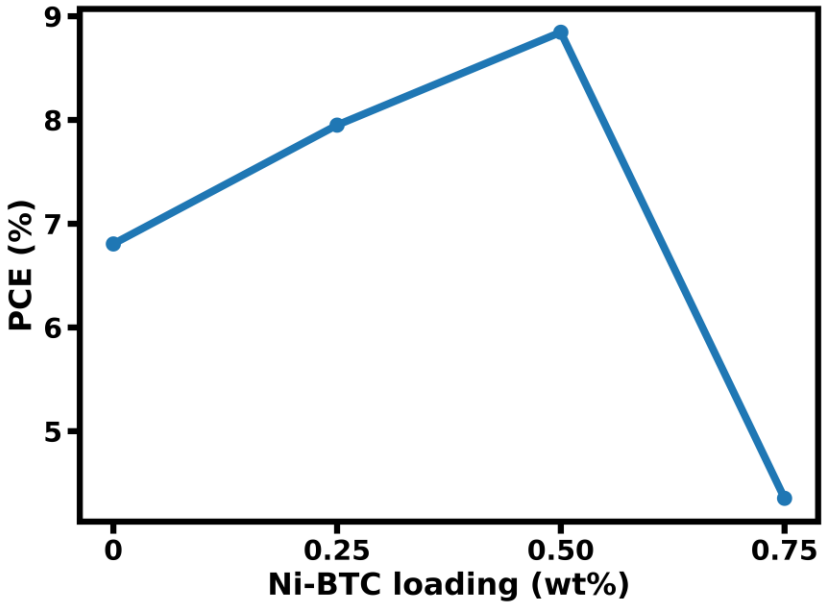


Fig. 9 Continuous PCHIP composition map for PCE and related optimization descriptors. The continuous PCE curve is an interpolation between measured anchors, not an independent experimental prediction.

Table 5. Retrospective device-level J–V model outputs.

Ni-BTC (wt%)	Voc measured (V)	Vmp model (V)	Jmp model (mA cm^{-2})	FF model	PCE model (%)
0	0.6380	0.3836	17.625	0.5280	6.7609
0.25	0.6270	0.3962	21.203	0.5330	8.4008
0.50	0.6240	0.3878	24.301	0.5160	9.4241
0.75	0.6050	0.4438	11.623	0.5760	5.1581

The reduced single-diode model reproduces the measured V_{oc} and J_{sc} by construction because these quantities are boundary conditions. Figure 10 shows the modelled J–V curves. The modelled FF values are 0.5280, 0.5665, 0.5528 and 0.6832, compared with measured values of 0.528, 0.533, 0.516 and 0.576. Consequently, the model overestimates FF most strongly for the 0.75 wt% device and should not be presented as a complete physical device model. Nevertheless, it retains the experimental PCE ranking and gives a retrospective PCE RMSE of 0.545 percentage points, MAE of 0.470 percentage points, MAPE of 7.84% and R^2 of 0.895.

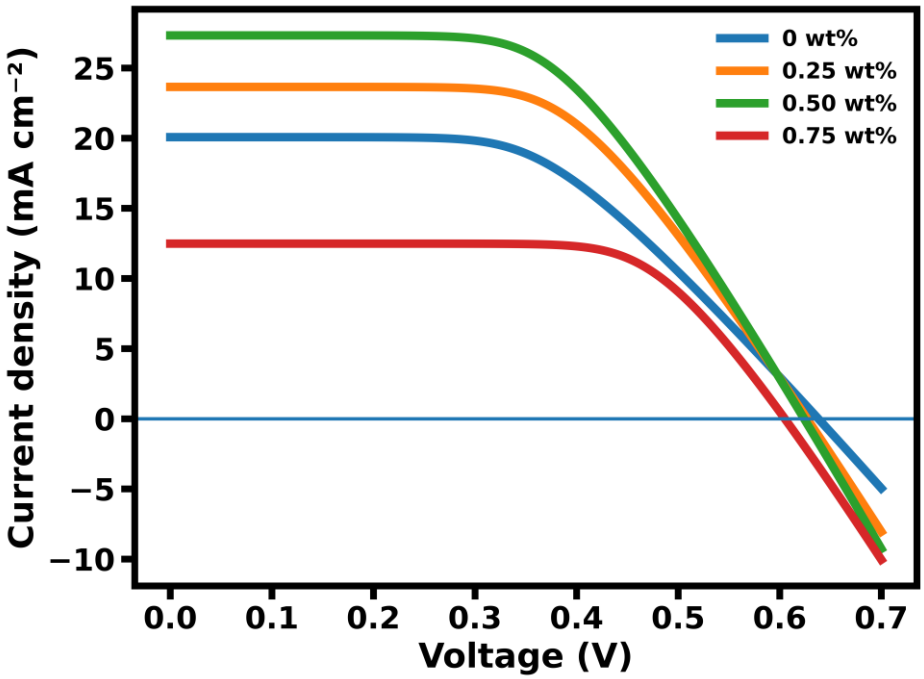


Fig. 10 Reduced device-level modelled J–V curves. Measured Jsc and Voc are boundary conditions; FF and PCE are forward-model outputs.

3.6 Digital twins and continuous optimisation

To assess the combined influence of optical properties, dye loading, interfacial charge transfer, and electron transport on the device performance, the key model-derived parameters were compared across the four Ni-BTC compositions. Table 6 summarises the corresponding results, providing a basis for interpreting the relationship between the individual mechanistic descriptors and the experimentally observed photovoltaic response. These comparisons help explain why 0.50 wt% Ni-BTC achieves the highest power conversion efficiency, whereas higher loading introduces substantial interfacial and electrolyte-transport limitations. The four digital twins show three regimes. The pristine state is transport-limited relative to the optimised state. The 0.25–0.50 wt% region is a high-performance regime in which interfacial resistance is reduced, and charge collection is improved. The 0.75 wt% state is a failure regime characterised by simultaneous increases in R_2 and R_3 despite an increased lifetime. Continuous interpolation identifies 0.50 wt% as the PCE and Jsc optimum because that point is itself an experimental anchor. A diagnostic balanced injection–transport window of approximately 0.352–0.547 wt% was obtained using transport ≥95% of its maximum and injection ≥80% of its maximum; these thresholds are analytical criteria rather than fitted physical constants.

Table 6. Four-composition digital-twin state vectors.

Ni-BTC (wt%)	Injection index	τn (ms)	R2 (Ω)	R3 (Ω)	Transport	Jsc	PCE
0	1.000	0.9253	25.70	17.1	1.000	20.07	6.805
0.25	5.160	1.1617	11.20	10.7	2.881	23.65	7.950
0.50	4.316	1.1617	9.81	10.9	3.289	27.32	8.846
0.75	3.176	1.4601	54.30	96.1	0.747	12.48	4.353

3.7 Uncertainty, sensitivity and prospective validation

To evaluate the robustness of the predicted optimum to uncertainty in the input parameters and model formulation, we performed Monte Carlo uncertainty propagation using 10,000 realisations. Table 7 summarises the resulting distributions of the predicted photovoltaic performance and optimum Ni-BTC loading. This analysis estimates the sensitivity of the model predictions to the specified uncertainty assumptions and helps assess the consistency of the identified optimum at 0.50 wt% Ni-BTC. The Monte Carlo analysis retained the 0.50 wt% PCE optimum in all 10,000 realisations under the stated uncertainty assumptions, while the maximum-PCE distribution had a mean of 8.8474% and a standard deviation of 0.1775 percentage points. The 95% model-propagated interval was 8.5054–9.1955%. This interval is not an experimental confidence interval because the input uncertainties were assumed rather than measured replicate errors. Interestingly, the optimum obtained from an injection-plus-transport diagnostic criterion was less stable (mean 0.341 wt%, with approximately 40.7% of realisations in the 0.35–0.55 wt% interval), reinforcing that the complete photovoltaic response contains additional constraints.

Table 7 Monte Carlo uncertainty-propagation results for 10,000 realisations.

Quantity	Monte Carlo result	Uncertainty summary	Interpretation
PCE optimum (wt%)	0.5000 in all 10,000 realisations	100%	Model-form + assumed relative uncertainty
Jsc optimum (wt%)	0.5000 in all 10,000 realisations	100%	Model-form + assumed relative uncertainty
Transport optimum (wt%)	mean 0.4917; median 0.50	95%: 0.25–0.50	Descriptor uncertainty
Balanced injection–transport optimum (wt%)	mean 0.3410; median 0.3325	95%: 0.25–0.50	Not equivalent to PCE optimum

Maximum PCE (%)	8.8474 ± 0.1775 (SD)	95%: 9.1955	8.5054–	Not an experimental confidence interval

Table 8. Retrospective validation metrics for the reduced device-level model.

Output	RMSE	MAE	MAPE (%)	R^2	Status
Jsc	0.0000	0.0000	0.0000	1.0000	Boundary condition
Voc	0.0000	0.0000	0.0000	1.0000	Boundary condition
FF	0.05908	0.04437	8.0069	-5.8014	Forward model; four-anchor retrospective validation
PCE	0.54487	0.46953	7.8374	0.8954	Forward model; four-anchor retrospective validation

A prospective validation framework was pre-defined without using new measurements. The current interpolation model is expected to yield PCE values of 8.410, 8.785, 8.846, 8.609, and 6.970% for target compositions of 0.35, 0.45, 0.50, 0.55, and 0.65 wt%, respectively. These values are hypotheses for future experiments, not validated predictions. The proposed acceptance criteria are PCE MAPE ≤10%, Jsc error ≤10%, lifetime error ≤10%, and the measured optimum within 0.45–0.55 wt%, with no parameter fitting before examining the validation data. The predictive performance of the reduced device-level model was assessed by comparing its outputs with the experimentally reported photovoltaic parameters. The corresponding retrospective validation metrics, including the relevant prediction errors, are presented in Table 8. These results quantify the agreement between the model and the experimental dataset while identifying the limitations of the simplified device-level description. As this evaluation uses the same experimental dataset that informed model development, it represents retrospective assessment rather than independent prospective validation.

4 Mechanistic interpretations

The integrated mechanism is summarised as Ni-BTC loading → TiO_2 structural evolution → optical/electronic modification → N719 injection → interfacial transfer (R_2) → electron lifetime/transport (τ_n/R_2) → electrolyte diffusion (R_3) → J_{sc}, Voc and FF → PCE. At low-to-moderate Ni-BTC content, reduced crystallite size and modified optical response accompany lower R_2 and improved charge collection. At 0.25 wt%, the modelled injection index is maximal, but the measured Jsc remains below that of 0.50 wt%, showing that injection is not the terminal bottleneck. At 0.50 wt%, the system reaches its most favourable combination of low R_2, moderate R_3, long lifetime and high current density. At 0.75 wt%, recombination lifetime alone appears favourable, but the 5.5-fold increase in R_2 relative to 0.50 wt% and the very high R_3 dominate the device response.

This interpretation is consistent with the broader DSSC literature, in which photoanode modification is effective only when optical harvesting, dye adsorption, charge injection, transport and recombination are simultaneously considered [4–6,9]. It also agrees with the parent experimental interpretation that R_2 is closely associated with electron transfer across the dye/TiO_2/electrolyte interface [1]. The present contribution therefore does not claim that one resistance parameter universally determines DSSC efficiency; rather, it provides a transparent quantitative framework for identifying which coupled descriptor becomes limiting within this particular four-composition dataset.

5 Limitations and prospective experimental validation

Several limitations should be made explicit. First, the model is based on four experimental compositions and therefore cannot establish universal composition–property laws. Second, absolute optical generation was not calculated because absorption coefficients and photoanode thickness were unavailable. Third, the conduction-band and N719 energetic descriptors used in the injection stage include digitisation and assumptions and should not be interpreted as new spectroscopic measurements. Fourth, the reduced *J–V* model uses measured J_{sc} and V_{oc} as boundary conditions and therefore cannot independently predict those quantities. Fifth, the Monte Carlo uncertainty distributions are scenario analyses based on assumed relative errors rather than experimental replicate statistics. The most direct next experiment is therefore to synthesise and test intermediate Ni-BTC loadings around 0.35–0.65 wt%, with particular emphasis on 0.45, 0.50 and 0.55 wt%. For each composition, *J–V*, EIS/Bode, dye loading, optical spectra and, where possible, transient photovoltage should be measured using the same device architecture and illumination conditions as in the parent study. The model should be evaluated prospectively against those observations before any recalibration. This procedure would convert the present interpolation framework into a genuinely predictive materials-design workflow.

6 Conclusions

A transparent multistage modelling framework was developed from the published Ni-BTC/TiO_2 aerogel DSSC dataset. The experimentally observed 0.50 wt% optimum is best interpreted as a coupled state rather than as the maximum of a single material property. The composition provides the lowest R_2 (9.81 Ω), a 1.1617 ms lifetime and the highest normalised τ_n/R_2 transport descriptor, yielding the highest measured Jsc (27.32 mA cm^{-2}) and PCE (8.846%). The 0.25 wt% sample illustrates the importance of downstream transport because it has the highest modelled injection index but not the highest J_{sc}. The 0.75 wt% sample demonstrates the opposite failure mode: a long lifetime is

overwhelmed by very high interfacial and electrolyte-diffusion resistances. Sensitivity and uncertainty analyses consistently identify interfacial resistance and coupled transport as critical variables. The resulting framework provides a reproducible basis for prospective experimental validation of intermediate Ni-BTC compositions and can be adapted to other modified semiconductor photoanodes.

References

1. V. Ramasubbu, P. Ram Kumar, E.M. Mothi, K. Karuppasamy, H.-S. Kim, T. Maiyalagan, X.S. Shajan, Highly interconnected porous TiO_2-Ni-MOF composite aerogel photoanodes for high power conversion efficiency in quasi-solid dye-sensitized solar cells. Appl. Surf. Sci. 496, 143646 (2019). https://doi.org/10.1016/j.apsusc.2019.143646

2. B. O'Regan, M. Grätzel, A low-cost, high-efficiency solar cell based on dye-sensitized colloidal TiO_2 films. Nature 353, 737–740 (1991). https://doi.org/10.1038/353737a0

3. A. Hagfeldt, G. Boschloo, L. Sun, L. Kloo, H. Pettersson, Dye-sensitized solar cells. Chem. Rev. 110, 6595–6663 (2010). https://doi.org/10.1021/cr900356p

4. K. Fan, J. Yu, W. Ho, Improving photoanodes to obtain highly efficient dye-sensitized solar cells: a brief review. Mater. Horiz. 4, 319–344 (2017). https://doi.org/10.1039/C6MH00511J

5. A.R.M. Khairudin, N.A.S. Aziz, M.Y.A. Rahman, A.A. Umar, Metal oxide and its modification as photoanode for dye-sensitized solar cell: a review. J. Mater. Sci.: Mater. Electron. 37, 936 (2026). https://doi.org/10.1007/s10854-026-17282-0

6. T. Rajaramanan, D. Velauthapillai, P. Ravirajan, M. Senthilnanthanan, A facile impregnation synthesis of Ni-doped TiO_2 nanomaterials for dye-sensitized solar cells. J. Mater. Sci.: Mater. Electron. 34, 916 (2023). https://doi.org/10.1007/s10854-023-10347-4

7. J.J. Pietron, A.M. Stux, R.S. Compton, D.R. Rolison, Dye-sensitized titania aerogels as photovoltaic electrodes for electrochemical solar cells. Sol. Energy Mater. Sol. Cells 91, 1066–1074 (2007). https://doi.org/10.1016/j.solmat.2007.02.021

8. Z. Inonu, S. Keskin, C. Erkey, An emerging family of hybrid nanomaterials: metal–organic framework/aerogel composites. ACS Appl. Nano Mater. 1, 5959–5980 (2018). https://doi.org/10.1021/acsanm.8b01428

9. B. Roose, S. Pathak, U. Steiner, Doping of TiO_2 for sensitized solar cells. Chem. Soc. Rev. 44, 8326–8349 (2015). https://doi.org/10.1039/C5CS00352K

10. Y.S. Kang, et al., Toward higher energy conversion efficiency for solid polymer electrolyte dye-sensitized solar cells: ionic conductivity and TiO_2 pore-filling. J. Phys. Chem. Lett. 5, 1249–1258 (2014). https://doi.org/10.1021/jz5002727

11. S.J. Lue, P.W. Lo, F.Y. Huang, K.W. Cheng, Y.L. Tung, Correlation between dye-sensitized solar cell performance and internal resistance using electrochemical impedance spectroscopy. J. Phys. Chem. Biophys. 5, 181 (2015). https://doi.org/10.4172/2161-0398.1000181

12. M. Grätzel, Dye-sensitized solar cells. J. Photochem. Photobiol. C 4, 145–153 (2003). https://doi.org/10.1016/S1389-5567(03)00026-1

Statements and Declarations

Funding

No new experimental funding is claimed for the present modelling study. The underlying experimental work was reported in the parent publication [1]. This modelling work was supported in part by the Thiagarajar College of Engineering, Madurai, through the Seed Money Research Grant (Sanction No. R&D Seed_Money/2025/7).

Competing interests

The authors declare that they have no relevant financial or non-financial interests to disclose.

Author contributions

E. R. Anishiya Chella Daisy: Methodology, software, simulation modelling, data curation, formal analysis, visualisation, and writing – original draft. P. Ram Kumar: Conceptualisation, experimental investigation, simulation workflow development, methodology, and writing – review and editing. X. Sahaya Shajan: Supervision, conceptualisation, project administration, and critical review and editing of the manuscript. All authors reviewed and approved the final manuscript.

Data availability

The experimental anchor data used in this modelling study are reported in Ref. [1].

Use of AI-assisted tools

The authors used generative AI-assisted tools during manuscript preparation for drafting, language organisation, and formatting. All scientific data, equations, calculations, interpretations, references and the final manuscript must be checked and approved by the authors, who retain full responsibility for the content.

Supplementary Files

This is a list of supplementary files associated with this preprint. Click to download.

- SupplementaryInformation.docx